

Microstructure, Cyclic Deformation and Corrosion Behavior of Laser Welded NiTi Shape Memory Wires

G.R. Mirshekari, A. Kermanpur, A. Saatchi, S.K. Sadrnezhad, and A.P. Soleymani

(Submitted December 21, 2014; in revised form May 28, 2015)

The present paper reports the effects of Nd:YAG laser welding on the microstructure, phase transformation, cyclic deformation behavior, and corrosion resistance of Ti-55 wt.% Ni wire. The results showed that the laser welding altered the microstructure of the weld metal which mainly composed of columnar dendrites grown epitaxially from the fusion line. DSC results indicated that the onset of the transformation temperatures of the weld metal differed from that of the base metal. Cyclic stress-strain behavior of laser-welded NiTi wire was comparable to the as-received material; while a little reduction in the pseudo-elastic property was noted. The weld metal exhibited higher corrosion potential, lower corrosion current density, higher breakdown potential and wider passive region than the base metal. The weld metal was therefore more resistant to corrosion than the base metal.

Keywords joint properties, laser welding, NiTi shape memory alloy

1. Introduction

Due to excellent functional and biomedical properties like shape memory, superelasticity, and biocompatibility effects, NiTi alloys have been used to make various medical instruments like orthopedic, dental, vascular, and cardiovascular devices (Ref 1-4). Because of their poor formability, the use of NiTi alloys has, however, been confined to simple and small components of the systems (Ref 5-7). Therefore, a suitable joining technique must be devised to help in the manufacturing of the devices and components with complex geometries.

In the past few years, several techniques have been investigated for joining NiTi alloys. Friction welding (Ref 8, 9), tungsten inert gas (TIG) welding (Ref 10), plasma welding (Ref 11), brazing (Ref 12, 13) and laser welding (Ref 14-18) are some examples. Among these diverse welding techniques, laser welding has been regarded as a suitable method for joining NiTi alloys, especially in the area of medical engineering, because of its ability to localize laser heat to a tiny spot resulting in small heat-affected and weld zones.

For the long-term use of NiTi as in microdevices or components, it is important to study the cyclic deformation

behavior of the joint after laser welding. However, few researchers have investigated the cyclic deformation behavior of the laser-welded NiTi. Alberty Viera et al. (Ref 18) showed that laser-welded NiTi cold roll plates exhibit superior functional, mechanical, and cyclic behaviors by presenting larger recoverable strain levels than the base material. On the contrary, Falvo et al. (Ref 19) demonstrated that due to the reduction in mechanical and shape memory performances, the NiTi-welded joints would not be suitable for the realization of smart components in constrained recovery applications, where a large strain must be recovered and a large tensile stress is induced. Furthermore, corrosion resistance of NiTi alloys is also important for their long-term use in implants and medical devices. In addition to the release of the metal ions into the physiological environment, the corrosion process would also result in the deterioration of the dimensional parameters of the corroding object. Geometrically complex small devices are susceptible to failure because of the corrosion (Ref 20). Choosing a method for fabrication of a medical device needs careful evaluation and optimization of the corrosion resistance. Besides, the corrosion resistance of human body joints is of great practical importance. Yet, little is known about this subject, especially for the welded structures. Chan et al. (Ref 21) showed that the pitting corrosion resistance of NiTi wires after laser welding is deteriorated. On the other hand, Yan et al. (Ref 22) revealed that NiTi alloy is less susceptible to pitting and crevice corrosion after laser welding due to the decrease in the number of carbides formed in the weld zone. In view of the contradictory results obtained from the previous studies, It is, therefore, essential to work more on the mechanical properties and corrosion resistance of the laser-welded NiTi alloy.

In the present study, the microstructure, phase-transformation temperatures, and cyclic stress-strain hysteresis of the laser-welded NiTi wires were investigated. Moreover, in order to evaluate the corrosion characteristics, the open circuit potential and potentiodynamic polarization tests were performed in the Ringer's physiological solution. The obtained results were compared to those of unwelded specimens for better judgment regarding the use of laser-welded NiTi in a specific application.

G.R. Mirshekari, A. Kermanpur, and A.P. Soleymani, Department of Materials Engineering, Isfahan University of Technology, 84156-83111 Esfahan, Iran; A. Saatchi, Department of Materials Engineering, Isfahan University of Technology, 84156-83111 Esfahan, Iran; and Department of Materials Science and Engineering, University of Wisconsin-Madison, Madison, WI 53706, USA; and S.K. Sadrnezhad, Department of Materials Science and Engineering, Sharif University of Technology, 11365-9466 Tehran, Iran. Contact e-mails: g.mirshekari@ma.iut.ac.ir and g.mirshekari@yahoo.com.

2. Experimental Procedures

Ti-55 wt.% Ni wires with diameter of 0.36 mm were used as raw material. The surfaces of wires were cleaned by immersing in a dilute hydrofluoric and nitric acid solution for 25 s to remove surface contaminants before laser welding. The wires were then ultrasonically cleaned in acetone bath for 10 min, followed by 5 min of cleaning in distilled water. Butt welding was made on two pieces of NiTi wires using Nd:YAG laser system (PIM-3475 model IQL-20) that produces a laser beam with a wavelength of 1064 nm. The laser welding process was performed under an argon shielding environment to prevent N₂, O₂, and H₂ from penetrating into the weld zone which can deteriorate the properties of the joint. The optimum laser welding parameters used in this study are listed in Table 1.

The samples were cold mounted and polished twice with 0.3 μm alumina powder and colloidal silica. The samples were then etched with HF:HNO₃:CH₃COOH (1:5:5) reagent for metallographic observations. Microstructural examinations and surface analysis were obtained using reflective light microscopy (RLM, Nikon, EPIPHOT 300) and scanning electron microscopy (SEM, model Philips XL30) equipped with the energy dispersive spectroscopy (EDS) system. The phase structures of both base and weld metals were identified by x-ray diffraction (XRD, Philips X Pert-MPD System) at 40 kV and 30 mA with Cu K_α radiation at room temperature.

Differential scanning calorimetry (DSC, NETZSCH 200 F3 Maia System) was used to study the phase-transformation behavior of the welded samples. Samples were cut out of the weld zone and the base metal in the weldment, 5.06 and 5.27 mg, respectively and then heated and cooled in the range from -100 to 100 °C at 10 °C/min.

Cyclic loading tests were carried out by the SANTAM-STM 50 test machine. Tests were done at low strain rate with a gauge length of 12.5 mm and cross-head displacement velocity of 1 mm/min at room temperature. The samples were subjected to 10 complete cycles of tensile loading to a maximum strain of 8% and subsequent unloading to zero force (with the same strain rate) without exertion of any pressure at the cycle end. The stress-strain hystereses were recorded automatically. Three specimens were evaluated for both the as-received and the laser-welded wires.

The electrochemical experiments were studied in the Ringer's physiological solution on both the base and the weld metal samples at 37 °C. The composition of the Ringer's physiological solution was listed as NaCl 0.86 g/100 mL, KCl 0.03 g/100 mL, CaCl₂·2H₂O 0.03 g/100 mL, Na⁺ 147 mEq/L, Ca⁺⁺ 4.5 mEq/L, K⁺ 4.1 mEq/L, Cl⁻ 155.7 mEq/L. These conditions simulate those prevailing in a human body. The electrochemical cell used was a standard three-electrode cell consisting of a working electrode, an Ag/AgCl reference electrode, and a platinum counter electrode. Prior to the electrochemical tests, the surfaces of the samples were degreased in acetone, followed by cleaning in distilled water, and finally dried thoroughly in air.

Two different electrochemical tests were performed: (i) the open circuit potential measurements and (ii) potentiodynamic polarizations using the Princeton Applied Research potentiostat (model PARSTAT 2273). The open circuit potentials were continuously measured for a period of 7 h, starting immediately after immersion in the electrolyte. The potentiodynamic polarization measurements were then made after 7-h immersion at the open circuit potential. The potential scan was started from 250 mV below the open circuit potential at a scan rate of 0.5 mV/s. In order to ensure reproducibility, each test was repeated three times. Surface morphologies of the samples after the potentiodynamic polarization tests were observed by SEM.

3. Results and Discussion

3.1 Microstructure

Transverse and lateral cross-sectional views of the laser-welded wires are shown in Fig. 1 and 2, respectively. The weld zone is mainly composed of columnar dendrites as shown in Fig. 1(b) as a result of rapid solidification and sufficient constitutional undercooling at the solid/liquid interface in laser welding (Ref 23). In addition, as can be seen in Fig. 1(c), epitaxial growth occurred in the weld zone adjacent to the fusion line. This kind of growth is beneficial to the welds, since it incorporates the weld zone to the grains from the base metal, preventing stress concentration at the interface. Similarities between crystal structures and chemical compositions of the weld zone and the base metal reveal the main characteristics of the solidification system and crystal growth (Ref 24). Figure 2 shows that the weld bead is free from any apparent welding defects.

Figure 3 depicts the XRD patterns of both the base and the weld metal samples. As can be seen, the peaks of austenitic B2 and martensitic B19' phases are observed in the base metal sample. However, laser welding eliminates the martensitic B19' phase from the structure of weld metal sample, being in the austenitic B2 phase. In fact, this phenomenon is due to rapid cooling rate and further solidification of the weld metal which would be changed by heat treatment of the sample. The small amounts of the rhombohedral R-phase and the Ni-Ti intermetallic phases that may be present in the system are not distinctly recognizable in the XRD patterns due to XRD technical limitations.

3.2 Phase-Transformation Temperatures

DSC curves (heating and cooling) of both the base and the weld metal samples are shown in Fig. 4. The transformation temperatures extracted from these curves are summarized in Table 2. The onset temperatures of the phase transformations are determined as the intersection of tangents to the slopes of a peak with the base line. The results indicate that both the base and the weld metal samples exhibit a two-step transformation including the formation of R-phase (rhombohedral phase)

Table 1 Laser welding parameters used for fabricating butt-welded joints

Maximum peak power, W	Frequency, Hz	Number of pulses	Laser pulse duration, ms	Pulse energy, J	Welding time, s	Laser spot diameter, mm	Gas flow, L/min	Gas pressure, atm
1000	3	15	3	3	5	0.8	26	1

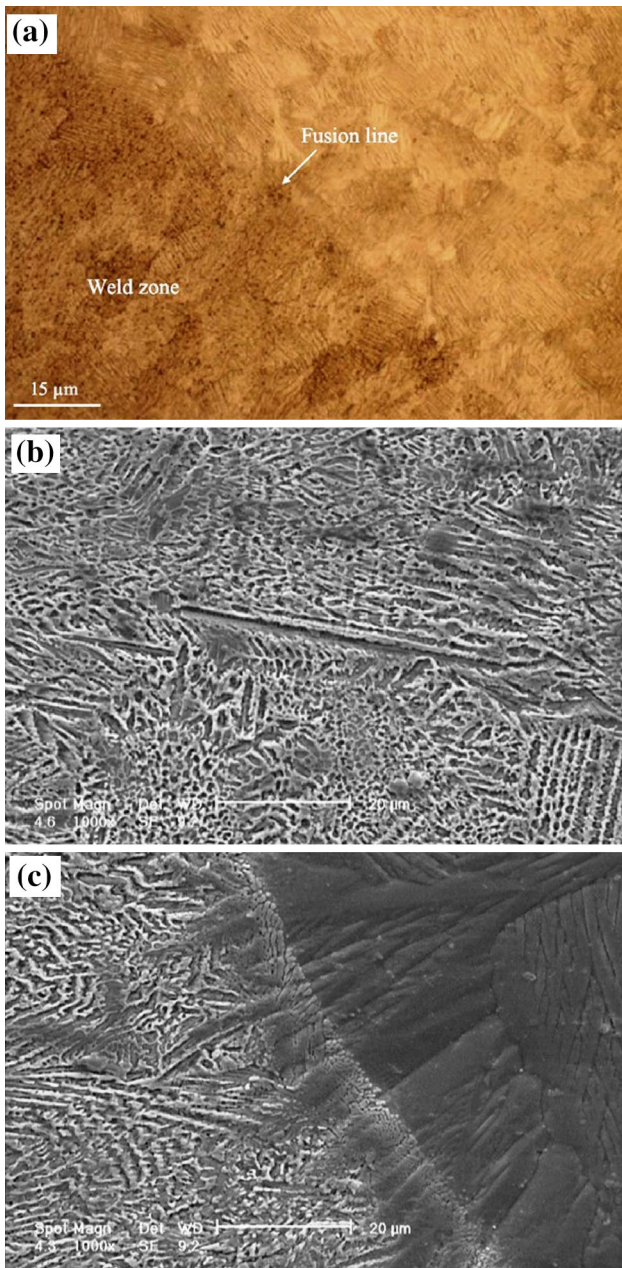


Fig. 1 (a) Transverse cross-sectional view of the welded structure. (b) Magnified view of the weld zone showing columnar dendrites. (c) Magnified view of the fusion line showing epitaxial growth

before B2 (austenite phase) formation from B19' (martensite phase) during heating half cycle. Moreover, the peaks related to the R-phase formation from B2 and transformation of R-phase to B19' are clearly observable in the DSC curve of weld metal during cooling half cycle. The R-phase usually competes before the austenite/martensite phase transformation. This phase is either totally absent, or appears during cooling before martensite formation. Thus, it gives a way to the martensitic transformation. Similarly, it may be absent during heating or may form prior to the martensite/austenite conversion. It usually exhibits a small shape memory or superelasticity effects within a narrow temperature range.

The temperatures for formation of the martensite are lower in the weld metal than in the base metal; while the reverse is

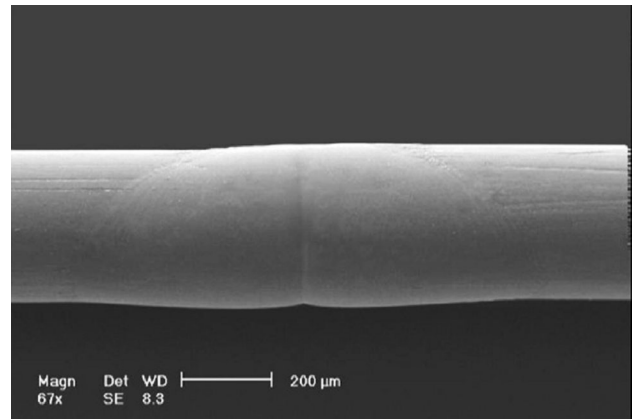


Fig. 2 Lateral cross-sectional view of the external part of laser-welded NiTi wire

true for the austenitic formation. Such alterations may originate from (i) the removal of the remained cold work originally present in the base metal and (ii) the creation of the thermally induced defects in the weld microstructure such as residual stress and grains growth. Such thermally induced defects could change the transition temperatures by hindering the phase reorientation during the phase change (Ref 23, 25). Biffi et al. (Ref 26) showed that the transformation temperatures can be also shifted even after the laser microcutting process due to the melting and subsequent rapid cooling.

There is no adequate evidence to identify the exact transformation pathway involved in the two-step transformation. The definitive information extracted from the DSC curves indicates that the base and the weld metals are in the purely B19' phase at very low temperatures and in the fully B2 phase at very high temperatures. At the intermediate temperatures, however, a mixture of B2, R, and B19' phases can be present in the system.

3.3 Cyclic Deformation Behavior

Previous study on the characteristic stress-strain curves obtained from static tensile testing for the as-received and the laser-welded NiTi wires showed that the stress-strain curve of the weldment basically followed the same path as that of the as-received sample with the characteristic behavior of a pseudo-elastic alloy and an ultimate tensile stress of 63% of the as-received wire (Ref 27). However, in terms of smart design involving superelasticity, a repeatable cyclic behavior along a loading-unloading path is required for a large number of cycles. In fact, in each cycle, changes in the microstructure and accumulation of residual strain occur, which tend to become stabilized over continuous transformation cycles, leading to the stabilization of the pseudo-elastic hysteretic response.

Figure 5 and 6 present the cycling stress-strain curves for the as-received and the laser-welded NiTi samples elongated up to strain of 8%, respectively. The stress-strain cycles of the samples exhibit typical features of austenitic NiTi, with the presence of a stress plateau, indicating the occurrence of stress-induced martensitic transformation (SIMT) and reorientation of the martensitic phases (Ref 28). The reversibility of these changes during unloading is the origin of the superelasticity of austenitic NiTi. In both Fig. 5 and 6, it is possible to verify the convergence of the hysteretic loops from the first cycles to the

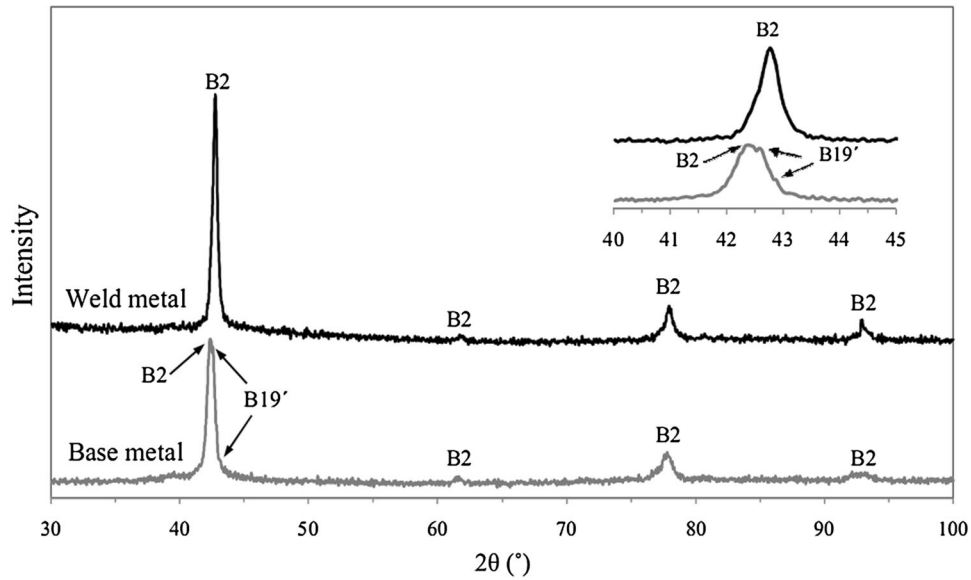


Fig. 3 XRD patterns of the base and the weld metal samples

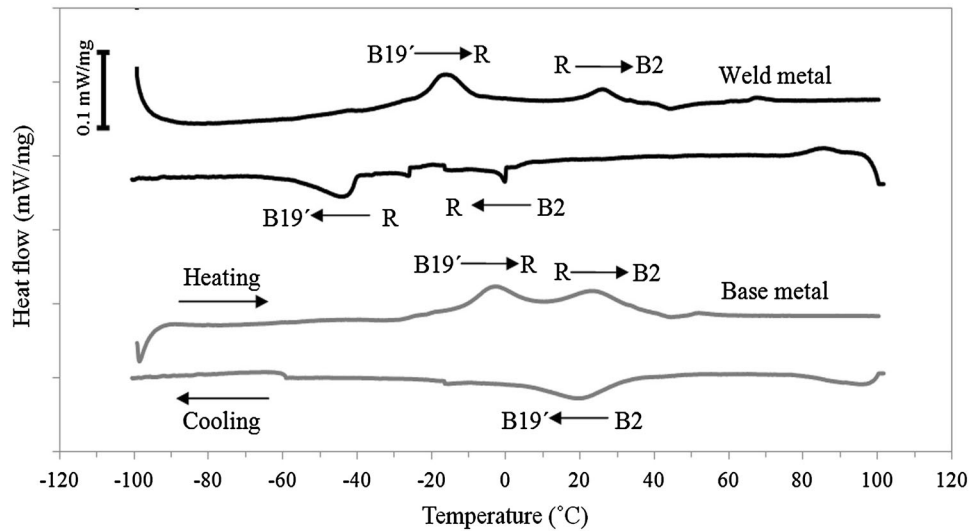


Fig. 4 DSC curves of the base and the weld metal samples

Table 2 Phase-transformation temperatures and enthalpies of the base and the weld metal samples

Samples	Transformation temperatures and enthalpies, °C, J/g							
	Heating curve				Cooling curve			
	A_s	A_p	A_f	ΔH	M_s	M_p	M_f	ΔH
Base metal	3.2	22.8	46.4	4.40	33.8	19.3	-1.3	-2.27
Weld metal	19.8	26.2	31.2	0.58	-39.7	-44.6	-57.9	-1.64

The transformation temperatures are denoted as A_s (austenite start), A_p (austenite peak), A_f (austenite finish), M_s (martensite start), M_p (martensite peak), M_f (martensite finish)

last ones. These results are consistent with those of previous authors (Ref 29-31), with the exception of faster gaining of the cyclic stability behavior which may be due to the compositional

and previous history differences in base metal samples. Also, the weld bead shows a softening effect in the starting and finishing of the stress plateau, resulting in more elongated

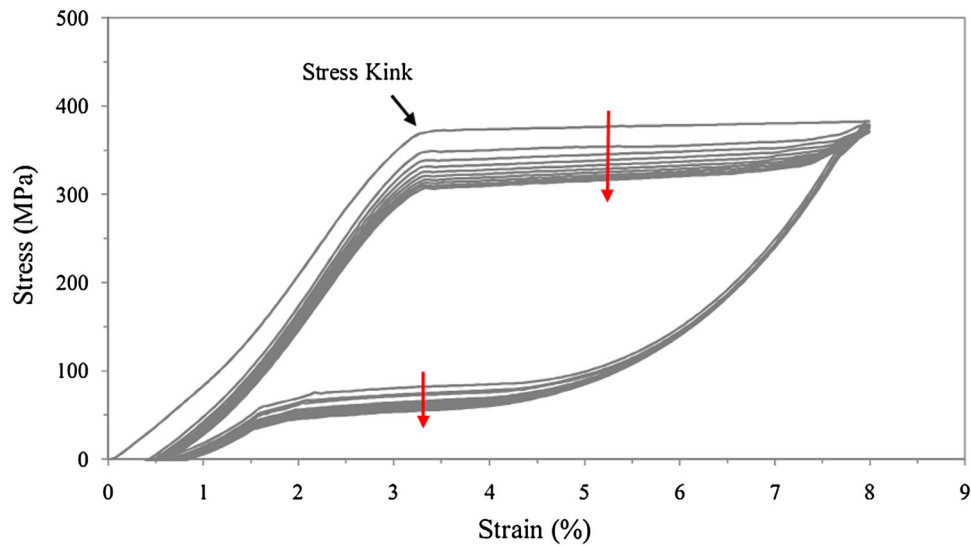


Fig. 5 Cyclic stress-strain hysteresis of the as-received sample up to strain of 8%

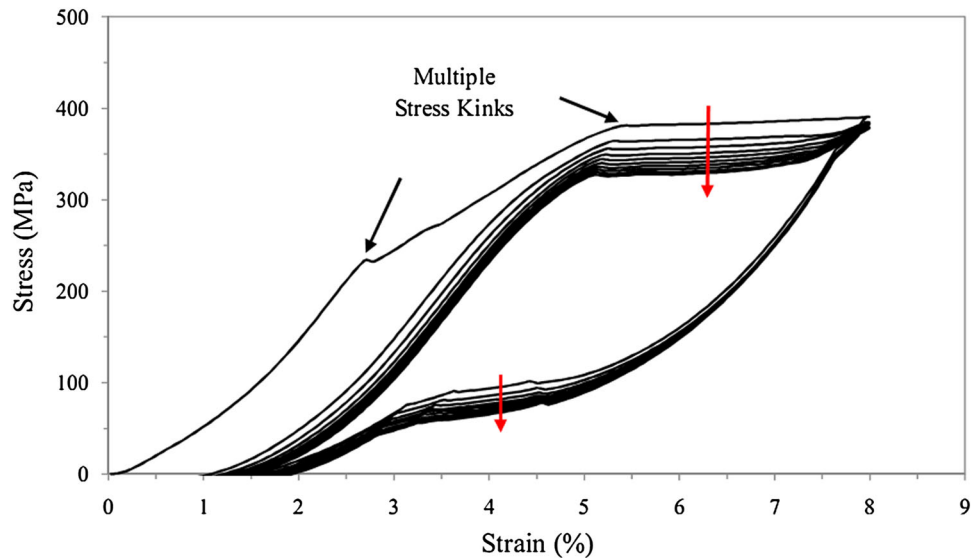


Fig. 6 Cyclic stress-strain hysteresis of the laser-welded sample up to strain of 8%

loops. As observed from the loading curves for the as-received sample in Fig. 5, a small stress kink is located ahead of the stress plateau. Such a stress kink usually indicates that a higher stress is required to overcome the barrier at the onset of the SIMT process (Ref 14). The stress-strain behavior of the weldment is much more complicated (Fig. 6). Compared with the as-received sample, the weldment exhibits multiple stress kinks in the first loading curve because the weldment is made up of different parts including weld zone, heat-affected zone (HAZ), and base metal, each with different transformation and superelastic behaviors. The stress kink prior to that ahead of the stress plateau in the first loading curve corresponds to the local and irreversible phase transformation in the weld zone.

The residual strain of the welded sample was accumulated differently from the as-received sample. To clarify this difference, a comparative study was carried out in order to evaluate the accumulated residual strains over successive

cycles, both in the as-received and the laser-welded specimens. The results are presented in Fig. 7 in terms of the accumulated residual strain. It can be seen that the as-received sample has a superior ability of strain recovering, presenting lower residual strains over the cycles than that of the laser-welded sample. This observation points to the fact that the accumulated residual strain of the weldment in the cyclic deformation test is dominated by the amount of plastic strain induced in the welded region due to the local SIMT (Ref 23).

3.4 Corrosion Behavior

Figure 8 shows the open circuit potentials of the base and the weld metal samples in the Ringer's physiological solution at 37 °C as a function of time. The aim of corrosion potential measurements is to understand the corrosion behavior of the specimens under equilibrium conditions in a simulated human

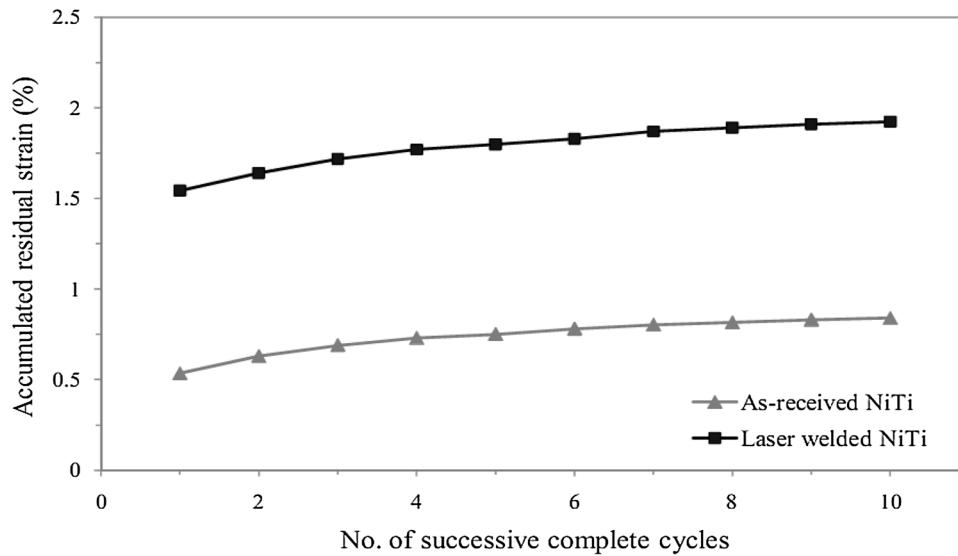


Fig. 7 Accumulated residual strains for the as-received and the laser-welded samples at different loading cycles

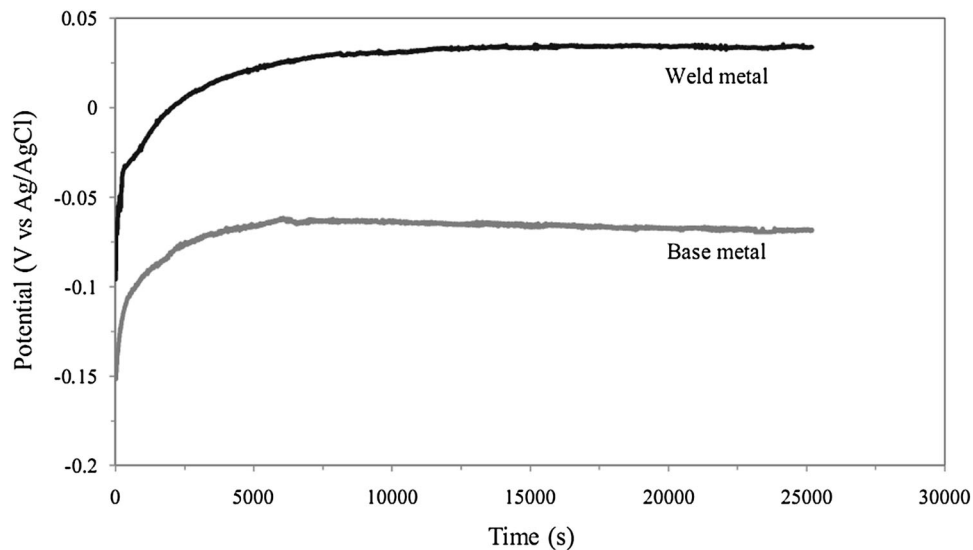


Fig. 8 Variations of the open circuit potentials of the base and the weld metal samples in the Ringer's physiological solution held at 37 °C for 7 h

body environment. As can be seen, the open circuit potential of the weld metal is about 100 mV higher than the base metal. This indicates that the protective oxide film which consists predominantly of a titanium oxide film (TiO_2), formed on the weld metal, is more stable than that formed on the base metal. This oxide film serves two purposes: (i) increasing the stability of the surface layer by protecting the bulk material from corrosion and (ii) creating a physical and chemical barrier against Ni ions release from the NiTi bulk material. The release of Ni ions to the surrounding bio-environments is a major problem for NiTi as a biomaterial, because Ni generates allergic reaction and has toxic effects on the cells if its concentration in the tissue exceeds certain levels (Ref 21, 32).

The representative potentiodynamic polarization curves of the base and the weld metal samples in the Ringer's physiological solution at 37 °C are shown in Fig. 9. The corrosion

current densities (i_{corr}), corrosion potentials (E_{corr}), and breakdown potentials (E_b) of the samples were determined from the potentiodynamic polarization curves (Tafel extrapolation method) and summarized in Table 3. As illustrated in Fig. 9 and Table 3, the weld metal exhibits higher corrosion resistance with lower corrosion current density ($0.03 \mu\text{A}/\text{cm}^2$) in comparison with the base metal. Also, the weld metal has higher corrosion potential (4 mV) than that of the base metal. Thus, when the base and the weld metals are adjacently placed together in the electrolyte, the weld metal is the cathodic part of the galvanic couple. Furthermore, the polarization curve of the base metal is characterized by a small passive region extending for about 750 mV from -150 to 600 mV. The end of the passive region represents the breakdown potential above which the passive film breaks down, and pits initiate on the surface. This is indicated by the rapid increase in the anodic current as a

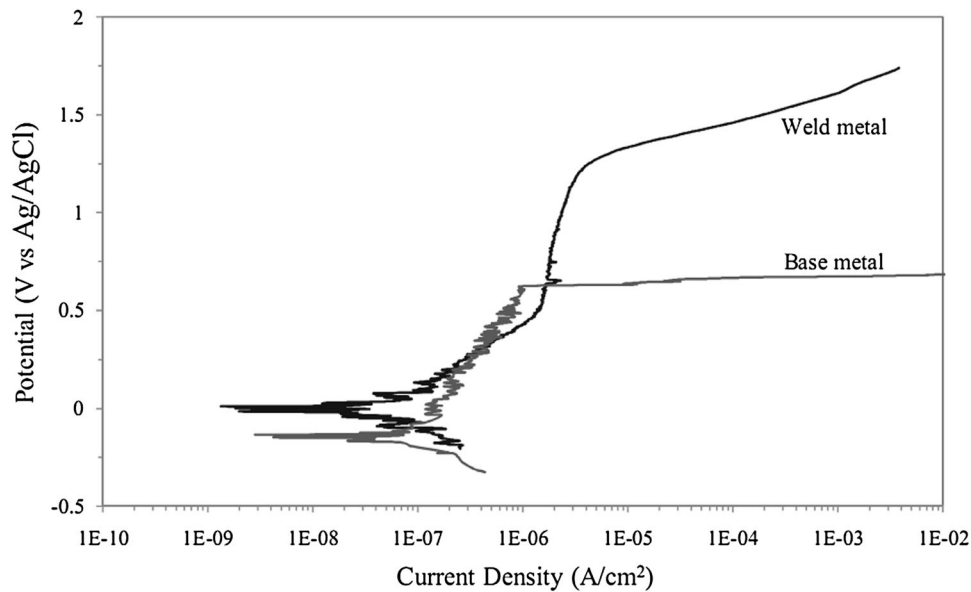


Fig. 9 Potentiodynamic polarization curves of the base and the weld metal samples in the Ringer's physiological solution at 37 °C

Table 3 Mean values of the electrochemical corrosion parameters obtained from potentiodynamic polarization curves for the base and the weld metal samples in the Ringer's physiological solution at 37 °C evaluated by the Tafel extrapolation method

Specimen	E_{corr} , mV	i_{corr} , $\mu\text{A}/\text{cm}^2$	E_b , mV
Base metal	-150	0.09	600
Weld metal	4	0.03	1250

Table 4 Surface compositions and Ti/Ni ratios of the base and the weld metal samples

Specimen	Ti, at.%	Ni, at.%	Ti/Ni ratio
Base metal	48.44	51.56	0.94
Weld metal	52	48	1.08

consequence of the passivity breakdown. The polarization curve for the weld metal shows a relatively wide passive region with breakdown potential of 1250 mV which is approximately 650 mV higher than that of the base metal. The obtained results show that the weld metal has better corrosion resistance than the base metal which are in good agreement with the findings of Yan et al. (Ref 17).

The surface quality is very important for NiTi alloy because it will strongly affect the nature of the passive film. One of the possible reasons for the better corrosion resistance of the weld metal could be related to the surface topography by which the smoother surface has a better corrosion resistance (Ref 33). In this study, as shown in Fig. 2, the weld metal has a clean appearance and smoother surface than the base metal. Moreover, as previously mentioned, the passivity of the NiTi alloy is mainly dependent on the Ti-rich surface oxide TiO_2 . Higher Ti/Ni ratio is usually beneficial for the formation of more stable TiO_2 film (Ref 21, 34). Therefore, better corrosion resistance of

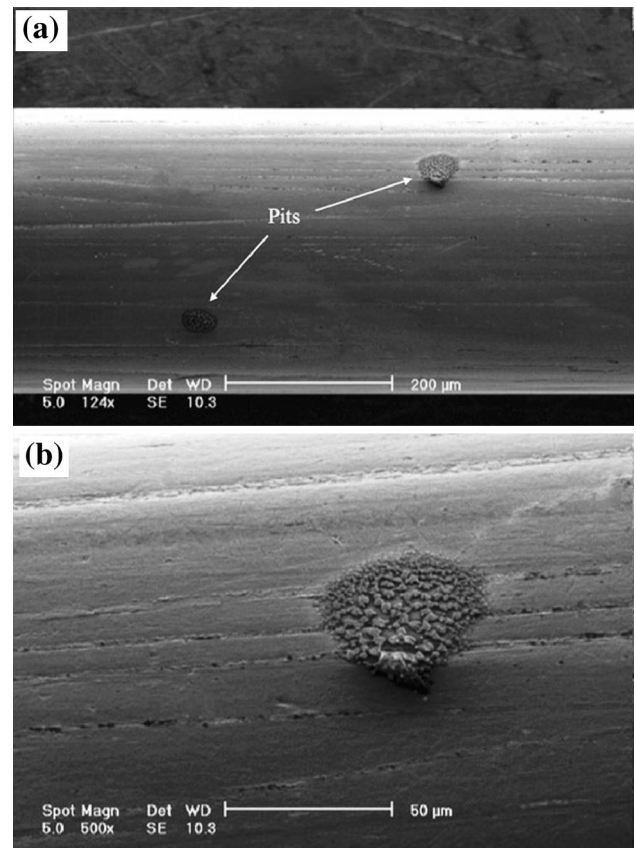


Fig. 10 Surface morphologies of the base metal after potentiodynamic polarization test: (a) at lower magnification and (b) at higher magnification showing the pits on the surface

the weld metal is also attributed to higher surface Ti/Ni ratio than the base metal, as shown in Table 4, ensuring the formation of a highly stable TiO_2 layer on the weld metal surface.

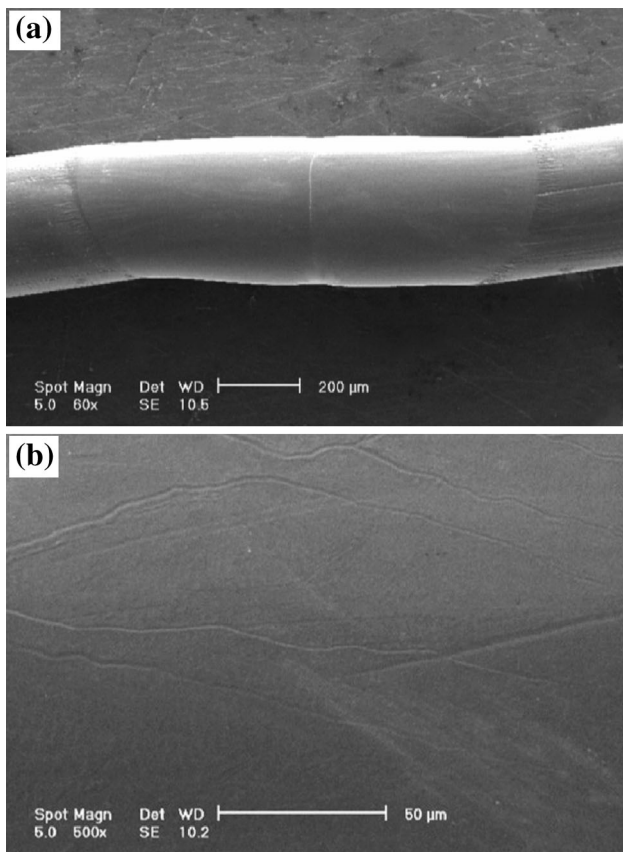


Fig. 11 Surface morphologies of the weld metal after potentiodynamic polarization test: (a) at lower magnification and (b) at higher magnification

The SEM images of the base and the weld metal samples after potentiodynamic polarization tests are shown in Fig. 10 and 11, respectively. After corrosion tests, pits could be observed on the surface of the base metal while for the weld metal, pits could not be observed clearly.

4. Conclusions

In this study, the effects of Nd:YAG laser welding on microstructure, phase-transformation behavior, cyclic stress-strain behavior, and corrosion resistance of NiTi wire were investigated. Laser welding was done with no major defects. The weld-zone structure consisted mainly of columnar dendrites which grew epitaxially from the weld boundary. Laser welding changed the phase structure of the laser-welded NiTi which was composed of B2 phase in the weld metal structure. The phase-transformation temperatures of the NiTi samples were changed after laser welding. Compared with the as-received NiTi wire, the laser-welded NiTi wire exhibited an increase in the stress required to trigger the martensitic transformation. Furthermore, the amount of the accumulated residual strain of the weldment was also increased. The weld metal exhibited better corrosion resistance than the base metal through higher corrosion potential, lower corrosion current density, a wider passive region, and higher breakdown potential than that of the base metal. It was confirmed by SEM

micrographs that pits could be observed obviously on the surface of the base metal, but not on the surface of the weld metal after potentiodynamic polarization tests. As a remarkable aspect, the results showed the possibility to join NiTi wires with desirable joint properties.

References

1. T. Duerig, A. Pelton, and D. Stockel, An Overview of Nitinol Medical Applications, *Mater. Sci. Eng. A*, 1999, **273–275**, p 149–160
2. N.B. Morgan, Medical Shape Memory Alloy Applications-The Market and Its Products, *Mater. Sci. Eng. A*, 2004, **378**, p 16–23
3. F. Nematzadeh and S.K. Sadmezhaad, Effects of the Ageing Treatment on the Superelastic Behavior of a Nitinol Stent for An Application in the Esophageal Duct: A Finite-Element Analysis, *Mater. Technol.*, 2013, **47(4)**, p 45–51
4. S.K. Sadmezhaad, N.H. Nemati, and R. Bagheri, Improved Adhesion of NiTi Wire to Silicone Matrix for Smart Composite Medical Applications, *Mater. Des.*, 2009, **30(9)**, p 3667–3672
5. S.K. Sadmezhaad and S.B. Raz, Effect of Microstructure on Rolling Behavior of NiTi Memory Alloy, *Mater. Manuf. Process.*, 2008, **23(7)**, p 646–650
6. X. Zhao, W. Wang, L. Chen, F. Liu, J. Huang, and H. Zhang, Microstructures of Cerium Added Laser Weld of a TiNi Alloy, *Mater. Lett.*, 2008, **62**, p 1551–1553
7. S.K. Sadmezhaad, N. Yasavol, M. Ganjali, and S. Sanjabi, Property Change During Nanosecond Pulse Laser Annealing of Amorphous NiTi Thin Film, *Bull. Mater. Sci.*, 2012, **35(3)**, p 357–364
8. T. Shinoda, T. Tsuchiya, and H. Takahashi, Functional Characteristics of Friction Welded Near-Equiatomic TiNi Shape Memory Alloy, *Trans. Jpn. Weld. Soc.*, 1991, **22**, p 30–36
9. S. Fukumoto, T. Inoue, S. Mizuno, K. Okita, T. Tomita, and A. Yamamoto, Friction Welding of TiNi Alloy to Stainless Steel Using Ni Interlayer, *Sci. Technol. Weld. Join.*, 2010, **15**, p 124–130
10. A. Ikai, K. Kimura, and H. Tobush, TIG Welding and Shape Memory Effect of TiNi Shape Memory Alloy, *J. Intell. Mater. Syst. Struct.*, 1996, **7**, p 646–654
11. C. Van der Eijk, H. Fostervoll, Z.K. Sallom, and O.M. Akselsen, Plasma Welding of NiTi to NiTi, Stainless Steel and Hastelloy C276, *Proceedings of the ASM Materials Solutions Conference*, Pittsburgh, Pennsylvania, October 13–15, 2003, p 125–129
12. M. Seki, H. Yamamoto, M. Nojiri, K. Uenishi, and K.F. Kobayashi, Brazing of Ti-Ni Shape Memory Alloy with Stainless Steel, *J. Jpn. Inst. Met.*, 2000, **64**, p 632–640
13. X.M. Qiu, M.G. Li, D.Q. Sun, and W.H. Liu, Study on Brazing of TiNi Shape Memory Alloy with Stainless Steels, *J. Mater. Process. Technol.*, 2006, **176**, p 8–12
14. H. Gugel, A. Schuermann, and W. Teisen, Laser Welding of NiTi Wires, *Mater. Sci. Eng. A*, 2008, **481–482**, p 668–671
15. A. Tuissi, S. Besseghini, T. Ranucci, F. Squatrito, and M. Pozzi, Effect of Nd-YAG Laser Welding on the Functional Properties of the Ni-49.6 at.% Ti, *Mater. Sci. Eng. A*, 1999, **273–275**, p 813–817
16. Y.H. Hsu, S.K. Wang, and C. Chen, Effect of CO₂ Laser Welding on the Shape-Memory and Corrosion Characteristics of TiNi Alloy, *Metall. Mater. Trans. A*, 2001, **32**, p 569–576
17. X.J. Yan, D.Z. Yang, and X.P. Liu, Corrosion Behavior of a Laser-Welded NiTi Shape Memory Alloy, *Mater. Charact.*, 2007, **58**, p 623–628
18. L. AlberyVieira, F.M. BrazFernandes, R.M. Miranda, R.J.C. Silva, L. Quintino, A. Cuesta, and J.L. Ocana, Mechanical Behaviour of Nd:YAG Laser Welded Superelastic NiTi, *Mater. Sci. Eng. A*, 2011, **528**, p 5560–5565
19. A. Falvo, F.M. Furguiele, and C. Maletta, Laser Welding of a NiTi Alloy: Mechanical and Shape Memory Behaviour, *Mater. Sci. Eng. A*, 2005, **412**, p 235–240
20. R. Venugopalan and C. Trépanier, Assessing the Corrosion Behaviour of Nitinol for Minimally Invasive Device Design, *Minim. Invasive Ther. Allied Technol.*, 2000, **9**, p 67–74

21. C.W. Chan, H.C. Man, and T.M. Yue, Effect of Post-Weld Heat-Treatment on the Oxide Film and Corrosion Behaviour of Laser-Welded Shape Memory NiTi Wires, *Corros. Sci.*, 2012, **56**, p 158–167
22. X.-J. Yan, D.-Z. Yang, and X.-P. Liu, Electrochemical Behavior of YAG Laser-Welded NiTi Shape Memory Alloy, *Trans. Nonferrous Met. Soc. China*, 2006, **16**, p 572–576
23. C.W. Chan, H.C. Man, and T.M. Yue, Effect of Postweld Heat Treatment on the Microstructure and Cyclic Deformation Behavior of Laser-Welded NiTi-Shape Memory Wires, *Metall. Mater. Trans. A*, 2012, **43A**, p 1956–1965
24. M.D.M. das Neves, A. Lotto, J.R. Berretta, W. de Rossi, and N.D.V. Junior, Microstructure Development in Nd:YAG Laser Welding of AISI, 304 and Inconel 600, *Weld. Int.*, 2010, **24**, p 739–748
25. C.W. Chan, H.C. Man, and T.M. Yue, Susceptibility to Environmentally Induced Cracking of Laser-Welded NiTi Wires in Hanks' Solution at Open-Circuit Potential, *Mater. Sci. Eng. A*, 2012, **544**, p 38–47
26. C.A. Biffi, P. Bassani, M. Carnevale, N. Lecis, A. Loconte, B. Previtali, and A. Tuissi, Effect of Laser Microcutting on Thermo-mechanical Properties on NiTiCu Shape Memory Alloy, *Met. Mater. Int.*, 2014, **20**, p 83–92
27. G.R. Mirshekari, A. Saatchi, A. Kermanpur, and S.K. Sadrnezhaad, Laser Welding of NiTi Shape Memory Alloy: Comparison of the Similar and Dissimilar Joints to AISI, 304 Stainless Steel, *Opt. Laser Technol.*, 2013, **54**, p 151–158
28. C. Maletta, E. Sgambitterra, F. Furgiuele, R. Casati, and A. Tuissi, Fatigue of Pseudoelastic NiTi Within the Stress-Induced Transformation Regime: A Modified Coffin-Manson Approach, *Smart Mater. Struct.*, 2012, **21**, p 112001
29. H. Tobushi, T. Nakahara, Y. Shimeno, and T. Hashimoto, Low-Cycle Fatigue of TiNi Shape Memory Alloy and Formulation of Fatigue Life, *Trans. ASME*, 2000, **122**, p 186–191
30. G. Eggeler, E. Hornbogen, A. Yawny, A. Heckmann, and M. Wagner, Structural and Functional Fatigue of NiTi Shape Memory Alloys, *Mater. Sci. Eng. A*, 2004, **378**, p 24–33
31. C. Maletta, E. Sgambitterra, F. Furgiuele, R. Casati, and A. Tuissi, Fatigue Properties of a Pseudoelastic NiTi Alloy: Strain Ratcheting and Hysteresis Under Cyclic Tensile Loading, *Int. J. Fatigue*, 2014, **66**, p 78–85
32. S.A. Shabalovskaya, Surface, Corrosion, and Biocompatibility Aspects of Nitinol as an Implant Material, *Bio-Med. Mater. Eng.*, 2002, **12**, p 69–109
33. H.H. Huang, Corrosion Resistance of Stressed NiTi and Stainless Steel Orthodontic Wires in Acid Artificial Saliva, *J. Biomed. Mater. Res.*, 2003, **66(4)**, p 829–839
34. C.W. Chan and H.C. Man, Laser Welding of Thin Foil Nickel-Titanium Shape Memory Alloy, *Opt. Lasers Eng.*, 2011, **49**, p 121–126